Excitation Spectral Phasor Microscopy (ExSPM) unveils spatiotemporal heterogeneities in polarity of intracellular lipid droplets

Jiayi Liu[1], Yi He[1], Rui Yan[2], Jinhong Yan[1], Ruirong Wang[1], Zhipeng Zhang[1], Jiankai Xia[1], Igor Kireev[3], Ke Xu[4], Kun Chen[1,5,*]

[1]School of Optoelectronic Science and Engineering, University of Electronic Science and Technology of China, Chengdu 610054, China

[2]Department of Genetics, Blavatnik Institute, Harvard Medical School, Boston, MA 02115, USA

[3]Belozersky Institute of Physico-chemical biology, Lomonosov Moscow State University, Leninskie Gory,1, Moscow 119991, Russia

[4]Department of Chemistry, University of California, Berkeley, CA 94720, USA

[5]Yangtze Delta Region Institute (Huzhou), University of Electronic Science and Technology of China, Huzhou 313000, China

*Correspondence to: chenk21@uestc.edu.cn

Abstract

Spatiotemporal heterogeneities in the polarity of intracellular LDs play essential roles in cellular function but remain largely unexplored. Here, we introduce excitation spectral phasor microscopy (ExSPM), which combines high-throughput excitation spectral imaging with phasor analysis to detect subtle spectral shifts of fluorophores in response to local intracellular environments with exceptional sensitivity and spatiotemporal resolution. Using the lipophilic dye Nile Red, we reveal substantial heterogeneities and dynamic changes in LD polarity within single mammalian cells. We further demonstrate LDs polarity is associated with lipid catabolism through lysosome-dependent acid lipophagy or neutral lipolysis at LDs–mitochondrion contact sites, underscoring its key role in cellular energy homeostasis. Additionally, ExSPM reveals that nutrient deprivation preferentially upregulates neutral lipolysis over acid lipophagy to meet cellular energy demands. Together, ExSPM provides a highly sensitive approach for resolving intricate spatiotemporal heterogeneities in intracellular composition and function, offering broad potential for the investigation of diverse cellular processes.

Introduction

Lipid droplets (LDs) are dynamic organelles essential for cellular lipid storage and

metabolism[1]. Beyond serving as reservoirs of neutral lipids, they actively interact with other organelles to regulate energy homeostasis and lipid signaling[2, 3]. Structurally, LDs consist of a core of nonpolar neutral lipids, such as triacylglycerol (TAG) and cholesterol, surrounded by a more polar phospholipid monolayer embedded with specialized surface proteins[4]. Once thought to be compositionally uniform, LDs are now recognized as highly heterogeneous across and within cell types, reflecting diverse energetic and metabolic demands[5, 6]. This structural and compositional diversity plays a crucial role in cellular function and is increasingly linked to metabolic regulation and disease[7]. A key factor underlying this heterogeneity is LD polarity, a fundamental biochemical parameter that governs the distribution of lipids, proteins, and enzymes[8]. Variations in LD polarity may influence lipid packing, phase separation, and surface protein interactions, ultimately regulating lipid storage, catabolism, and intracellular trafficking[9, 10]. These polarity-driven differences contribute to the functional diversity of LDs, highlighting their dynamic role in cellular physiology.

Fluorescence solvatochromic dyes, such as Nile Red and its derivatives, offer a powerful means to probe LD polarity due to their red-shifted fluorescence in polar environments[11-13]. Recent studies employing these dyes have revealed significant polarity differences among normal and cancer cells, various cancer types, muscle-damaged cells, and liver lesion cells[9, 10, 14, 15]. These findings offer new insights into LD composition and function while highlighting their potential as diagnostic markers for disease detection. While LD polarity varies across cell types, its intracellular characterization remains largely unexplored, despite its critical role in metabolic adaptation and cellular functions. Even within a seemingly homogeneous population, individual LDs can exhibit distinct polarity profiles influenced by their proximity to organelles, developmental stage, localized metabolic conditions, or transient stressors (e.g., nutrient gradients, oxidative hotspots). Recently, a subset of LDs associated with mitochondria was found to undergo novel liquid-crystalline phase transitions[16] and facilitate the transfer of harmful proteins to mitigate mitochondrial damage[17]—both processes likely driven by polarity changes that influence cellular survival. Thus, deciphering spatiotemporal variations in intracellular LD polarity is essential for understanding their morphological, chemical, and compositional heterogeneities, as well as the dynamic metabolic microenvironments that drive cellular function and disease progression. A recent study employing newly synthesized LD probes identified intracellular polarity differences but lacked sufficient sensitivity and temporal resolution to resolve the underlying mechanisms[13].

Addressing this challenge requires advanced imaging techniques capable of resolving subtle LD polarity variations with high spatial and temporal resolutions. Current approaches using solvatochromic dyes primarily rely on ratiometric fluorescence measurements with two excitation or emission channels[10, 12, 13, 15], limiting their sensitivity to subtle intracellular differences. While point-scanning spectral imaging can capture full emission spectra to enhance sensitivity to spectral variations[11], it imposes substantial constraints on temporal resolution. Unlike emission-based methods, we previously developed high-throughput excitation spectral microscopy (ExSM), which rapidly scans frame-synchronized excitation wavelengths for the entire

imaging field to acquire wavelength-resolved images[18-20]. This approach enables spectral unmixing to quantify fluorophore abundances, facilitating novel imaging strategies for bi-state biosensors. However, spectral unmixing cannot disentangle multi-state biosensors, such as polarity-sensitive dyes with full-color solvatochromic fluorescence, as their spectra shift continuously rather than consisting of discrete states.

To overcome these limitations, we here developed Excitation Spectral Phasor Microscopy (ExSPM), a technique that integrates high-throughput excitation fluorescence spectral microscopy with phasor analysis. ExSPM detects subtle spectral responses of fluorophores to local intracellular environments without prior spectral knowledge, enabling the direct visualization of intracellular spatiotemporal heterogeneities. Using the lipophilic fluorophore Nile Red, ExSPM reveals rich heterogeneities and dynamic variations in LD polarity, regulated by lipid metabolism and cellular energy homeostasis. These findings underscore ExSPM's transformative potential to advance our understanding of spatiotemporal heterogeneities in intracellular composition and function.

Results

Spectral phasor analysis is a non-fitting, Fourier-based method for extracting information from fluorescence lifetime[21], and more recently fluorescence spectral imaging[22, 23]. By converting high-dimensional spectral data into a 2D phasor space, it enables visualization of pixel ensembles, revealing population distributions and interpixel correlations inaccessible to fitting analysis[24]. Widely used in multiplexed fluorescence microscopy, it excels in spectral unmixing, compression, denoising, and computational efficiency[23]. Here, we repurpose phasor analysis for excitation spectral microscopy (ExSPM) to start assessing its multiplexing performance in five-color intracellular imaging. Using eight excitation wavelengths based on our previously reported ExSM setup[18, 20], spectrally overlapping fluorophores labeling five distinct subcellular targets were successfully unmixed with minimal crosstalk by leveraging linear additivity in phasor space (Fig. S1 and the Supplementary Note 1 for details). While spectral phasor analysis is well-established for multi-color imaging, it has been rarely used to characterize subtle fluorophore spectral shifts. We demonstrate ExSPM's exceptional sensitivity in detecting these variations, unveiling spatiotemporal heterogeneities that governs composition and function of LDs.

ExSPM unveils distinct compositional polarity heterogeneity of LDs within cells. Intracellular LDs are highly dynamic organelles central to lipid metabolism, membrane synthesis, and lipid-derived signaling. We started with Nile Red, a solvatochromic lipid dye commonly used to report changes in the chemical polarity of lipids in cells[11, 25-27]. Previous studies based on emission spectral shifts showed that mitochondrial and endoplasmic reticulum (ER) membranes are more polar and structurally less ordered than the plasma membrane, exhibiting red-shifted fluorescence[26]. In this study, we examined the excitation spectra of Nile Red on different membranes in live COS-7 cells (Supplementary Fig. S2). Cells were imaged in a buffer containing a high concentration of Nile Red (3.3 μM), ensuring that the cell plasma membrane and the membranes of

intracellular organelles were well labeled and visualized. Consistent with prior findings, mitochondrial and ER membranes showed redder shifts relative to the plasma membrane, while LDs exhibited the most blue-shifted excitation spectra, indicating lower polarity and a more ordered phase. The excitation spectra of Nile Red dissolved in solvents of various known polarities also demonstrate the spectral shifts depending on solvent polarity (Supplementary Fig. S2c). Interestingly, some LDs also exhibited unexpected red-shift spectra (the magenta arrow in Supplementary Fig. S2).

To understand the substantial polarity heterogeneities of individual LDs, we then utilized ExSPM to examine potential changes in the underlying excitation spectra of Nile Red at high spectral and spatial resolutions. At a low concentration (30-50 nM), Nile Red preferentially stained LDs over cell membranes (Fig. 1a and Supplementary Fig. S3), minimizing interference from other structures. The phasor plot of the spectral images grouped pixels with similar spectral profiles into clusters, enabling direct visual inspection of potential spectral shifts without prior spectral knowledge (Fig. 1b, where G and S are the real and imaginary coefficients). Unexpectedly, the phasor plot exhibited a broad distribution in G-S space, suggesting spatial heterogeneities within LDs, with a subset in the lower-right plane potentially indicating distinct polarity. Revisiting the excitation spectra of six LDs within the cell (marked with arrows in Fig. 1a), we found notable differences, including a striking ~60 nm blue shift from LD1 to LD6 (Fig. 1c).

To present both spectral and spatial information for each LD, we calculated the phase angle of each pixel and used this value to map it onto a continuous color scale (160° – 290°). Physically, the phase angle (ϕ=arctan(S/G)) is linear with the mean wavelength (the center of mass of the excitation spectrum) from spectral phasor transformation (Fig. 1c and Supplementary Note 1). Accordingly, a small phase angle denotes blue-shift spectrum corresponding to low polarity and ordered phases in LDs. The resultant "true-color" images revealed striking spectral differences among LDs (Fig. 1c and d, and Supplementary Fig. S3 and S4) with a strong phase shift up to 130°. This extensive dynamic range, coupled with ExSPM's high-throughput spectral detection, enables the identification of LD subpopulations with distinct polarities, allowing for highly sensitive mapping of LD compositional and functional heterogeneities across entire cells at high spatiotemporal resolutions.

While red-shifted, polarized LDs are randomly scattered throughout the cytoplasm in some cells (Fig. 1f, Supplementary Fig. S4 and S5), they were predominantly localized to the perinuclear region in most cells (Fig. 1d and 1e, Supplementary Fig. S3 and S5). The fraction of red-shifted LDs varied significantly between cells (Supplementary Fig. S5), indicating substantial compositional and functional heterogeneity. Additionally, many LDs also exhibited a polarity gradient from core to surface (Fig. 1g-i, Supplementary Fig. S3 and S4), consistent with prior ratiometric studies showing that triglyceride-rich cores are less polar than phospholipid monolayers. To further explore this, we analyzed fluorescence intensity variations among LDs with different polarities. Statistical analysis of >1,000 LDs from Fig. 1d and 1f revealed that LDs with smaller phase angles (lower polarity) were brighter, while red-shifted LDs were dimmer (Fig. 1j and Supplementary Fig. S3). This aligns with Nile Red's known

behavior of exhibiting higher quantum yield in nonpolar environments. Furthermore, LD polarity did not show a strong correlation with LD size (Fig. 1k and Supplementary Fig. S4).

ExSPM unveils the spatiotemporal heterogeneities in polarity of LDs in live cells. We next harnessed our above capability to map the spatiotemporal dynamics of LD polarity in live cells. Through continuous recording under our 8-wavelength excitation scheme at 10 fps and performing phasor analysis for every pixel, we obtained full-frame LD polarity images at 0.8 s time resolution (Fig. 2a-c, Supplementary Fig. S6, Video 1 and 2). This approach revealed diverse polarity dynamics among individual LDs within a single cell. LDs, as highly dynamic organelles, frequently undergo fission and fusion events critical for lipid biogenesis and catabolism. During LD–LD fusion, we observed a gradual polarity decrease (Fig. 2d-e, Supplementary Fig. S6 and Video 3), whereas fission led to increased polarity (Fig. 2f-g, Supplementary Fig. S6 and Video 4). These changes likely reflect shifts in the concentration of nonpolar lipids, such as cholesterol and TAG—fusion concentrates these lipids, reducing polarity, while fission dilutes them, increasing polarity. Even within individual LDs, polarity fluctuated significantly (230° – 260°) over 1-2 minutes (Supplementary Fig. S6e-g), indicating ongoing compositional changes. Notably, fixed cells exhibited the same polarity characteristics and heterogeneities as live cells (Supplementary Fig. S7), suggesting that LD compositions remain stable following chemical fixation.

LDs exhibit significant mobility (Fig. 2h, Supplementary Video 5), with slow movements appearing random and diffusional, while fast movements are more directional (Fig. 2i and 2j). Using the particle tracker model (MosaicSuite)[28], we tracked individual LDs (color-coded in Fig. 2i) and quantified their velocities. One-step movement analysis of each LDs (Fig. 2k) revealed that high-polarity LDs tend to move faster (orange arrows in Fig. 2j), while low-polarity LDs predominantly move more slowly (cyan arrows in Fig. 2j), a correlation evident in Supplementary Videos 5 and 6. The rapid, directional motion of high-polarity LDs likely reflects their association with microtubules, which mediate LD transport for various cellular functions[29]. In contrast, the slower, random movement of low-polarity LDs suggests they diffuse freely within the cytoplasm. An additional hypothesis is lysosome-LD interactions during lipophagy may enhance LD mobility, as lysosomes have been reported to move at twice the speed of LDs[30] (see more discussions below).

ExSPM unveils that LDs polarity is closely linked to cellular energy metabolism. We next asked whether LD polarity is influenced by energy metabolism in live cells. Cells typically maintain lipid metabolism and energy homeostasis by activating fatty acid oxidation during starvation and promoting lipogenesis under nutrient-rich conditions. To assess metabolic effects on LD polarity, COS-7 cells were cultured in full-serum medium (10% fetal bovine serum, FBS, Fig. 3a, e, and i), FBS-starvation medium (Fig. 3b, f, and j), or oleic acid (OA)-supplemented media (Fig. 3c-d, g-h, and k-l). Under starvation, LD polarity remained heterogeneous but showed an overall increase compared to full-serum conditions (Fig. 3b and Supplementary Fig. S8),

marked by a phase angle shift corresponding to a red-shifted fluorescence (Fig. 3e vs. Fig. 3f). Statistical analysis of tens of thousands of LDs across hundreds of cells further validated this trend (Fig. 3j). Conversely, excess OA led to increased LD accumulation and significantly reduced polarity, both in full-serum (Fig. 3c, g, and k) and FBS-starvation medium (Fig. 3d, h, and l). Higher OA concentrations and longer treatments further amplified this effect (Supplementary Fig. S8c-h and Fig. S9). Similar polarity changes were observed in HeLa and A549 cells (Fig. 3m), though intrinsic differences were noted. HeLa cells consistently exhibited higher average LD polarity compared to COS7 and A549 cells under all tested conditions (Fig. 3m, and Supplementary Fig. S10 and Fig. S11).

These results suggest that nutrient deprivation, which promotes TAG hydrolysis to generate free fatty acids (FFAs) for mitochondrial β-oxidation[31], increases LD polarity to support cellular energy demands. In contrast, the reduction in LD polarity observed with lipid stimuli likely reflects the detoxifications of FFAs with enhanced storage of nonpolar TAG and cholesterol within LDs[32]. HeLa cells, as cancer cells, appear to rely more on lipid catabolism for energy homeostasis, exhibiting consistently higher LD polarity. Together, these findings indicate that spatiotemporal heterogeneities in LD polarity are closely linked to lipid catabolism and may regulate various metabolic processes. The release of FFAs from LDs through ester hydrolysis, a process known as lipolysis[33], implies that coordination and interaction between LDs and other organelles are essential. This raises an intriguing question: do high LD polarity states correspond to specific stages or pathways of lipolysis?

ExSPM unveils high-polarity LDs as a hallmark of lysosome-dependent acid lipolysis (lipophagy). Lipolysis, a primary pathway for LD breakdown, occurs via cytoplasmic neutral lipolysis or acid lipolysis, the latter also known as lipophagy[31, 33]. In lipophagy, autophagosomes selectively engulf LDs and fuse with lysosomes, where lysosomal acid lipase hydrolyzes TAG and cholesterol to release FFAs for energy production. Additionally, lysosomes can directly interact with LDs to facilitate lipid transfer and hydrolysis[34]. To examine whether lysosome-associated LDs in lipophagy exhibit high polarity, we performed ExSPM of Nile Red, followed by cell fixation and immunofluorescence staining with the lysosome marker LAMP1 (Supplementary Fig. S12). As expected, in normal COS-7 cells, low-polarity LDs showed no colocalization with lysosomes, whereas most high-polarity LDs were marked by lysosomes (red arrows in Supplementary Fig. S12). However, under OA treatment, high-polarity LDs were nearly absent, and low-polarity LDs were largely excluded from lysosomes (Supplementary Fig. S12h-m).

To confirm that high-polarity LDs were authentic LDs and not lysosomes erroneously labeled by Nile Red, we utilized LipidSpot488 (LS488), a highly specific LD dye with minimal background staining of membranes or other organelles. LS488 was validated to exhibit no signal overlap with Nile Red under short excitation wavelengths, ensuring precise LD identification (Supplementary Fig. S13). The experimental workflow included sequential ExSPM imaging of Nile Red, followed by imaging of LAMP1 and LS488 in the same fixed cells (Fig. 4a). This strategy enabled

quantitative polarity mapping and accurate colocalization analysis through multi-fluorophore imaging.

In normal cells, most Nile Red-labeled droplets were also stained by LS488, displaying a broad spectral range from blue-violet to red-orange. This confirms the heterogeneity of LD polarity within cells (Fig. 4a, Supplementary Fig. S14). Colocalization with lysosomes revealed that LS488-only LDs were predominantly low in polarity (cyan arrows in Fig. 4b), whereas LDs labeled by both LS488 and lysosomes had higher polarity and reduced LS488 brightness (orange arrows in Fig. 4b). A subset of lysosome-only LDs exhibited the highest polarity and lacked LS488 signals entirely (red arrows in Fig. 4b and Supplementary Fig. S14). Statistical analysis of the phase angle across multiple cells confirmed a gradual increase in LD polarity following lysosomal fusion (Fig. 4c). These results may suggest a model in which neutral lipids, such as TAG and cholesterol, undergo hydrolysis, leading to increased LD polarity. This shift is accompanied by a progressive loss of LS488 signal, likely due to its inability to stain highly polar lipids and potential fluorescence quenching in the acidic lysosomal environment. Under FBS starvation, nutrient deprivation led to increased lysosome formation and enhanced lysosome-mediated lipophagy (Fig. 4d, white arrows indicated free lysosomes in Fig. 4e). Consequently, more lysosome-associated high-polarity LDs emerged (orange and red arrows in Fig. 4e, Fig. 4f and Supplementary Fig. S15), further supporting the model of polarity increase during lipophagy.

To directly assess lipophagy activity in FBS-starved cells, we used a lipophagy probe consisting of mCherry and EGFP tandem-tagged to livedrop, an LD-specific marker in which EGFP fluorescence is selectively quenched in acidic lysosomes[34, 35]. Multi-color ExSM imaging of mCherry-EGFP-livedrop and PhiYFP-LAMP1 revealed a significant increase in red puncta under FBS starvation (Fig. 4g and Supplementary Fig. S16). These red puncta colocalized with lysosomes (red arrows in Fig. 4g), confirming enhanced lipophagy flux. Together, these results demonstrate that lipophagy involves lysosomal fusion with LDs, leading to progressive lipid hydrolysis and increased LD polarity. However, some high-polarity LDs did not colocalize with lysosomes (cyan arrows, upper panel in Fig. 4e), suggesting that alternative, lysosome-independent pathways may also contribute to LD breakdown under nutrient deprivation.

ExSPM unveils high-polarity LDs as a hallmark of neutral lipolysis through LD-mitochondria contacts. The discovery of adipose triglyceride lipase (ATGL) established cytoplasmic neutral lipolysis as a key pathway for triacylglycerol hydrolysis, generating diacylglycerols and FFAs[33]. This process is closely linked to mitochondrial FFA uptake and oxidation, requiring LD-mitochondria proximity[31, 36, 37]. To examine the impact of direct LD-mitochondria contacts on LD polarity, we performed ExSPM imaging of Nile Red, followed by concurrent imaging of mitochondria and LS488 in the same cells (Fig. 5a-d). In normal cells, LDs lacking mitochondrial contact predominantly exhibit low polarity, whereas a subset of mitochondria-associated LDs display higher polarity (Supplementary Fig. S17). This effect is more pronounced under FBS starvation, where high-polarity LDs increasingly contact with mitochondria (orange and red arrows in Fig. 5e-f and Supplementary Fig. S18). While most of these

LDs retained LS488 staining, some did not, suggesting near-complete lipid hydrolysis. Notably, some high-polarity LDs labeled by LS488 lacked direct mitochondrial contact (white arrows in Fig. 5g), implying lysosome-mediated lipophagy as an alternative pathway. In contrast, low-polarity LDs in FBS-starved cells rarely interact with mitochondria (cyan arrows in Fig. 5 and Supplementary Fig. S18). Quantitative analysis further confirmed the significant impact of direct mitochondrion-LD contacts on increased LD polarity (Fig. 5h). This polarity shift may be further associated with liquid-crystalline phase transitions in LDs, as recently demonstrated[16], driven by the consumption of TAG metabolites for mitochondrial respiration at LD-mitochondria contact sites under starvation. Additionally, in OA-treated cells, where LDs predominantly exhibit low polarity, LDs and mitochondria remain largely segregated (Supplementary Fig. S19). These findings suggest that neutral lipolysis at LD-mitochondria contact sites, alongside lysosome-mediated lipophagy, plays a key role in shaping LD polarity. Importantly, both pathways are co-regulated by metabolic factors such as mTOR, AMPK, and FOXO[33], likely functioning as interconnected lipid catabolic processes that collectively influence LD polarity and regulate key signaling pathways in energy homeostasis.

ExSPM reveals nutrient deprivation preferentially upregulates intracellular neutral lipolysis over acid lipophagy. While both pathways contribute to lipid catabolism, it is not surprising that cells can dynamically regulate their usage for LD hydrolysis depending on metabolic conditions. To further understand how cells fine-tune pathway selection, we analyzed LD polarity from concurrent imaging of Nile Red and lysosomes, filtering out high-polarity LDs (phase angle > 240°) as actively hydrolyzing. Among these, LDs co-localizing with lysosomes were classified as undergoing acid lipophagy, while the rest were categorized as undergoing neutral lipolysis.

Statistical analysis revealed that in normal COS-7 cells, approximately 29% of LDs likely underwent active lipolysis, with lysosome-mediated lipophagy—rather than neutral lipolysis—dominating LD breakdown (~70%, Fig. 5i, left). This suggests that basal lipid mobilization during fed or early fasting states may prioritize lysosomal degradation to maintain metabolic homeostasis. Strikingly, during acute nutrient deprivation, the fraction of lipolytic LDs increased to 67%, with both acid lipophagy and neutral lipolysis synergistically upregulated in a coordinated response to increased energy demands. However, prolonged starvation shifted the balance toward neutral lipolysis (46%), bringing it closer to lysosome-mediated lipophagy (54%) and challenging the prevailing view that chronic stress universally favors autophagy.

Compared to COS-7 cells, HeLa cells exhibited consistently higher lipid catabolism under both nutrient-rich (62%) and deprivation (99%) conditions, with a stronger reliance on lysosome-mediated lipophagy (92% and 73%, respectively). A549 lung cancer cells, while maintaining low lipid catabolism under nutrient-rich conditions similar to COS-7 cells, showed a marked increase in lipolysis upon nutrient deprivation. In both conditions, A549 cells, like HeLa cells, depended more on lysosome-mediated lipophagy than COS-7 cells. Despite these differences, both HeLa and A549 cells

exhibited a similar shift in LD catabolism, with neutral lipolysis increasing more than acid lipophagy (Fig. 5i, middle and right). This shift may reflect endogenous lysosomal resource competition, where cells prioritize lysosomal capacity for protein and organelle recycling while reactivating cytosolic lipases to maintain FFA flux. During nutrient deprivation, global autophagy increases to degrade diverse substrates (e.g., via mitophagy, ribophagy), all requiring lysosomal acidification. This shared demand likely creates a bottleneck for acid lipophagy, which depends on lysosomal hydrolases, whereas neutral lipolysis, mediated by cytosolic lipases (e.g., ATGL, HSL), operates independently of lysosomal capacity.

Discussion

ExSPM, integrating high-throughput excitation fluorescence spectral microscopy with phasor analysis, provides highly sensitive detection of subtle spectral responses of fluorophores to local environments, enabling the visualization of intracellular heterogeneities at high spatial and temporal resolutions. Spectral phasor analysis, a non-fitting approach, extracts spectral information by converting high-dimensional data into a 2D phasor space, facilitating direct visual inspection of spectral shifts. This makes ExSPM ideal for imaging fluorophores with unknown or subtle spectral variations. Methodologically, it not only provides a highly sensitive tool but also redefines the capabilities of traditional fluorophores, potentially broadening the scope of biosensing for a wider range of cellular molecules and physicochemical parameters.

Biologically, ExSPM revealed intricate spatiotemporal heterogeneities within LDs, challenging the conventional view of LDs as uniform lipid reservoirs. While a recent study using newly synthesized LD probes identified polarity differences, its ratiometric approach lacked sensitivity and temporal resolution, leaving the underlying mechanisms unexplored[12, 13]. Our findings establish LD polarity as a functional marker of lipid metabolism, with high-polarity LDs associated with lipid catabolism and low-polarity LDs linked to lipid storage and detoxification. Live-cell imaging further revealed that LD polarity dynamically shifts during fusion, fission, and intracellular transport, highlighting the functional specialization of LD subpopulations.

Notably, LDs undergoing lysosome-mediated lipophagy exhibited a progressive increase in polarity, while LDs interacting with mitochondria also showed polarity shifts, implicating both acid and neutral lipolysis in lipid turnover. These findings suggest that LD polarity is not only a readout of metabolic activity but also a key determinant of LD function in cellular energy homeostasis. We quantified the contributions of these two major lipolysis pathways to understand how cells fine-tune pathway selection in response to varying energetic and metabolic demands. Contrary to conventional models, while both acid lipophagy and neutral lipolysis were upregulated, our findings reveal a paradigm shift in LD hydrolysis dynamics under nutrient stress, with a significantly stronger induction of neutral lipolysis compared to acid lipophagy in both cancer and normal cells. This shift may reflect lysosomal resource competition. Tissue-specific regulatory cues, such as hormonal signaling or autophagy-lysosomal efficiency[38], and LD remodeling (e.g., changes in size[39] or perilipin composition[6]), likely contribute to this transition. This compartmentalized regulation may also imply

that bulk autophagy can suppress specific selective autophagy subtypes under energetic stress, with cells prioritizing rapid lipid mobilization via parallel pathways during acute nutrient deprivation. Quantitatively, cancer cells, such as HeLa cells, exhibit higher levels of lipid catabolism to sustain their cellular energy demands, with this elevated catabolic activity relying more heavily on lysosome-mediated lipophagy.

Future investigations into the molecular mechanisms governing LD polarity, as well as the bidirectional interplay between lipolysis pathways—such as interactions with lipases[40], lipid transporters[41], and organelles[2, 3]—could further refine our understanding of lipid catabolism. Additionally, integrating ExSPM's temporal resolution and AI-driven spectral analysis may enable automated, high-throughput metabolic monitoring[42]. By providing a direct, quantitative measure of LD composition and dynamics, ExSPM offers new insights into lipid storage, mobilization, and metabolic regulation, with broad implications for cellular energy homeostasis and lipid-associated metabolic diseases.

Together, ExSPM has unveiled rich compositional and functional heterogeneities within intracellular LDs. By applying this spectral imaging method to a broader range of probes, particularly those traditionally considered environment-insensitive, it opens additional exciting possibilities for exploring cellular organizations and functions.

Acknowledgments

This work was supported by the National Natural Science Foundation of China (62205048, 62475032).

Author Contributions

K.C. conceived the research. J.L. designed and conducted the experiments. All authors contributed to experimental designs, data analysis, and paper writing.

Competing interests

The authors declare no competing financial interests.

References

1. Martin, S. & Parton, R.G. Lipid droplets: a unified view of a dynamic organelle. *Nature reviews Molecular cell biology* **7**, 373-378 (2006).
2. Olzmann, J.A. & Carvalho, P. Dynamics and functions of lipid droplets. *Nature reviews Molecular cell biology* **20**, 137-155 (2019).
3. Drizyte-Miller, K., Schott, M.B. & McNiven, M.A. Lipid droplet contacts with autophagosomes, lysosomes, and other degradative vesicles. *Contact* **3**, 2515256420910892 (2020).
4. Walther, T.C., Chung, J. & Farese Jr, R.V. Lipid droplet biogenesis. *Annual review of cell and developmental biology* **33**, 491-510 (2017).
5. Herms, A. *et al.* Cell-to-cell heterogeneity in lipid droplets suggests a mechanism to reduce

lipotoxicity. *Current Biology* **23**, 1489-1496 (2013).
6. Majchrzak, M. *et al.* Perilipin membrane integration determines lipid droplet heterogeneity in differentiating adipocytes. *Cell Reports* **43** (2024).
7. Onal, G., Kutlu, O., Gozuacik, D. & Dokmeci Emre, S. Lipid droplets in health and disease. *Lipids in health and disease* **16**, 1-15 (2017).
8. Yang, Z. *et al.* Macro-/micro-environment-sensitive chemosensing and biological imaging. *Chemical Society Reviews* **43**, 4563-4601 (2014).
9. Ventura, A.E. *et al.* Cell lipid droplet heterogeneity and altered biophysical properties induced by cell stress and metabolic imbalance. *Biochimica et Biophysica Acta (BBA)-Molecular and Cell Biology of Lipids* **1868**, 159347 (2023).
10. Pu, Y. *et al.* Multimode evaluating the fluctuation of lipid droplets polarity in acute kidney injury and tumor models. *Sensors and Actuators B: Chemical* **380**, 133343 (2023).
11. Teo, W. *et al.* Nile Red fluorescence spectroscopy reports early physicochemical changes in myelin with high sensitivity. *Proceedings of the National Academy of Sciences* **118**, e2016897118 (2021).
12. Collot, M. *et al.* Probing polarity and heterogeneity of lipid droplets in live cells using a push–pull fluorophore. *Analytical chemistry* **91**, 1928-1935 (2018).
13. Aknine, N. & Klymchenko, A.S. Push–pull fluorescent dyes with trifluoroacetyl acceptor for high-fidelity sensing of polarity and heterogeneity of lipid droplets. *Analytical Chemistry* **96**, 13242-13251 (2024).
14. Hu, J. *et al.* High-fidelity carbon dots polarity probes: revealing the heterogeneity of lipids in oncology. *Light: Science & Applications* **11**, 185 (2022).
15. He, D. *et al.* Ketocyanine-Based Fluorescent Probe Revealing the Polarity Heterogeneity of Lipid Droplets and Enabling Accurate Diagnosis of Hepatocellular Carcinoma. *Advanced Healthcare Materials* **13**, 2303212 (2024).
16. Mahamid, J. *et al.* Liquid-crystalline phase transitions in lipid droplets are related to cellular states and specific organelle association. *Proceedings of the National Academy of Sciences* **116**, 16866-16871 (2019).
17. Jin, Y., Tan, Y., Wu, J. & Ren, Z. Lipid droplets: a cellular organelle vital in cancer cells. *Cell death discovery* **9**, 254 (2023).
18. Chen, K., Yan, R., Xiang, L. & Xu, K. Excitation spectral microscopy for highly multiplexed fluorescence imaging and quantitative biosensing. *Light: Science & Applications* **10**, 97 (2021).
19. Chen, K., Li, W. & Xu, K. Super-multiplexing excitation spectral microscopy with multiple fluorescence bands. *Biomedical Optics Express* **13**, 6048-6060 (2022).
20. Yan, J., He, Y. & Chen, K. Excitation Spectral Microscopy for Highly Multiplexed Intracellular Imaging via Quasi-Blind Unmixing. *ACS Photonics* **11**, 3454-3466 (2024).
21. Ranjit, S., Malacrida, L., Jameson, D.M. & Gratton, E. Fit-free analysis of fluorescence lifetime imaging data using the phasor approach. *Nature protocols* **13**, 1979-2004 (2018).
22. Cutrale, F. *et al.* Hyperspectral phasor analysis enables multiplexed 5D in vivo imaging. *Nature methods* **14**, 149-152 (2017).
23. Chiang, H.J. *et al.* HyU: Hybrid Unmixing for longitudinal in vivo imaging of low signal-to-noise fluorescence. *Nature Methods* **20**, 248-258 (2023).
24. Malacrida, L., Ranjit, S., Jameson, D.M. & Gratton, E. The phasor plot: a universal circle to advance fluorescence lifetime analysis and interpretation. *Annual Review of Biophysics* **50**, 575-

593 (2021).
25. Kucherak, O.A. *et al.* Switchable nile red-based probe for cholesterol and lipid order at the outer leaflet of biomembranes. *Journal of the American Chemical Society* **132**, 4907-4916 (2010).
26. Moon, S. *et al.* Spectrally resolved, functional super-resolution microscopy reveals nanoscale compositional heterogeneity in live-cell membranes. *Journal of the American Chemical Society* **139**, 10944-10947 (2017).
27. Sarkar, A., Mitra, J.B., Sharma, V.K., Namboodiri, V. & Kumbhakar, M. Spectrally Resolved Single-Molecule Orientation Imaging Reveals a Direct Correspondence between the Polarity and Microviscosity Experienced by Nile Red in Supported Lipid Bilayer Membranes. *The Journal of Physical Chemistry B* (2025).
28. Rizk, A. *et al.* Segmentation and quantification of subcellular structures in fluorescence microscopy images using Squassh. *Nature protocols* **9**, 586-596 (2014).
29. Nardi, F. *et al.* Lipid droplet velocity is a microenvironmental sensor of aggressive tumors regulated by V-ATPase and PEDF. *Laboratory Investigation* **99**, 1822-1834 (2019).
30. Valm, A.M. *et al.* Applying systems-level spectral imaging and analysis to reveal the organelle interactome. *Nature* **546**, 162-167 (2017).
31. Rambold, A.S., Cohen, S. & Lippincott-Schwartz, J. Fatty acid trafficking in starved cells: regulation by lipid droplet lipolysis, autophagy, and mitochondrial fusion dynamics. *Developmental cell* **32**, 678-692 (2015).
32. Singh, R. *et al.* Autophagy regulates lipid metabolism. *Nature* **458**, 1131-1135 (2009).
33. Zechner, R., Madeo, F. & Kratky, D. Cytosolic lipolysis and lipophagy: two sides of the same coin. *Nature Reviews Molecular Cell Biology* **18**, 671-684 (2017).
34. Schulze, R.J. *et al.* Direct lysosome-based autophagy of lipid droplets in hepatocytes. *Proceedings of the National Academy of Sciences* **117**, 32443-32452 (2020).
35. Pu, M. *et al.* ORP8 acts as a lipophagy receptor to mediate lipid droplet turnover. *Protein & cell* **14**, 653-667 (2023).
36. Wang, J. *et al.* An ESCRT-dependent step in fatty acid transfer from lipid droplets to mitochondria through VPS13D− TSG101 interactions. *Nature communications* **12**, 1252 (2021).
37. Ghorpade, M., Rajput, D., Mahalingam, P. & Kanvah, S. Live cell imaging of lipid droplets: fluorescent chalcones as probes for lipophagy and lipid–mitochondria interactions. *Journal of Materials Chemistry B* **13**, 1338-1349 (2025).
38. Yang, Q. *et al.* Regulation of lipolysis by 14-3-3 proteins on human adipocyte lipid droplets. *PNAS nexus* **2**, pgad420 (2023).
39. Klemm, R.W. & Carvalho, P. Lipid droplets big and small: Basic mechanisms that make them all. *Annual Review of Cell and Developmental Biology* **40**, 143-168 (2024).
40. Kintscher, U., Foryst-Ludwig, A., Haemmerle, G. & Zechner, R. The role of adipose triglyceride lipase and cytosolic lipolysis in cardiac function and heart failure. *Cell Reports Medicine* **1** (2020).
41. Wong, L.H., Gatta, A.T. & Levine, T.P. Lipid transfer proteins: the lipid commute via shuttles, bridges and tubes. *Nature reviews Molecular cell biology* **20**, 85-101 (2019).
42. Liu, X., An, H., Cai, W. & Shao, X. Deep learning in spectral analysis: Modeling and imaging. *TrAC Trends in Analytical Chemistry*, 117612 (2024).

Figures

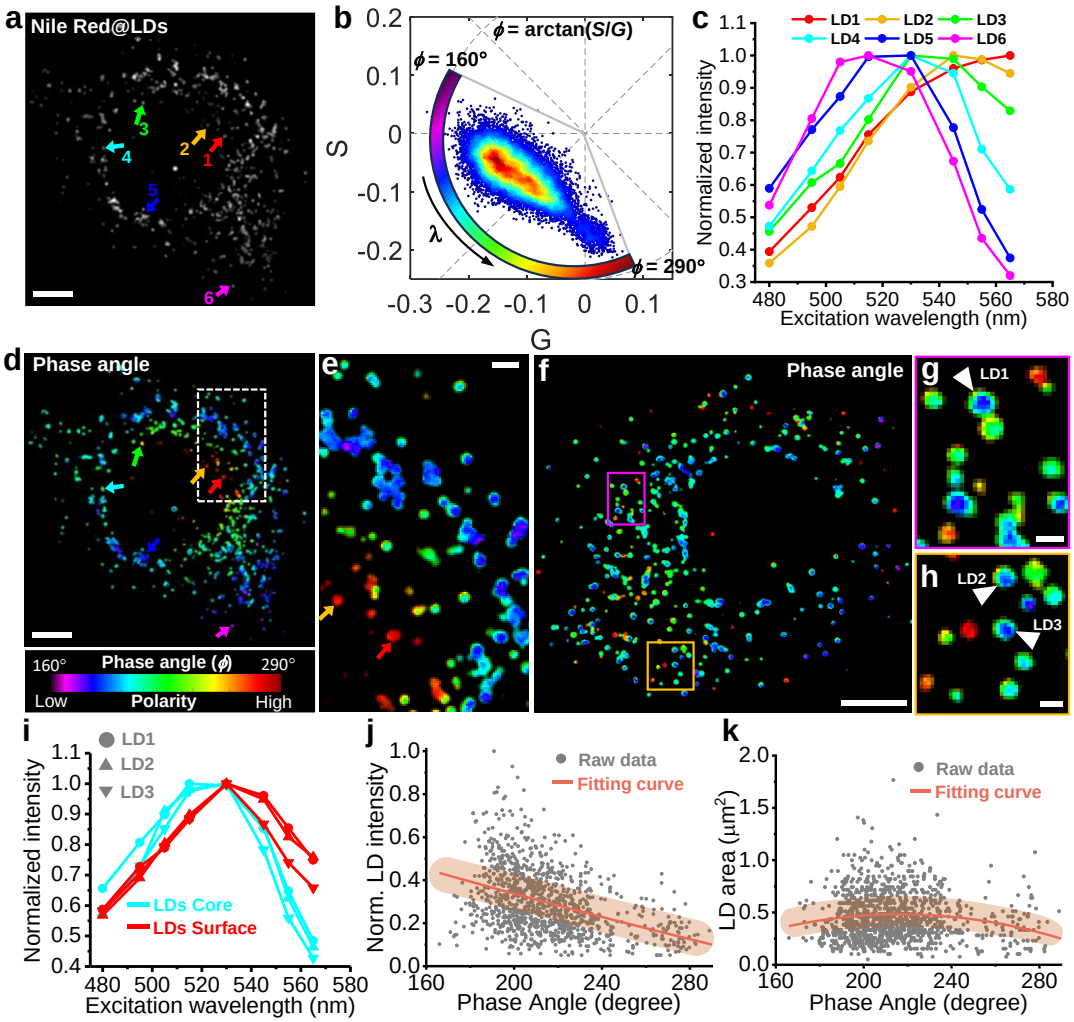

Figure 1. ExSPM unveils distinct compositional polarity heterogeneity of LDs within cells. a. Conventional fluorescence image of LDs stained with Nile Red at a low concentration (30 nM) in a COS-7 cell. **b.** ExSPM represents excitation spectral data as a phasor plot, a 2D histogram of the real (*G*) and imaginary (*S*) Fourier components at a single harmonic. **c.** Excitation spectra of six individual LDs indicated by arrows in a. **d.** High-resolution polarity mapping of intracellular LDs, color-coded by the phase angle derived from the phasor plot in b. **e.** Magnified view of the white-boxed subregion in d. **f.** An LD polarity map of another cell obtained with ExSPM. **g, h.** Zoomed-in views of the boxed regions in f. **i.** Spectral differences between the core and surface of three LDs marked by arrowheads in. **j.** Distributions of the measured phase angles and fluorescence intensities for single LDs. **k.** Distributions of the measured phase angles and areas for single LDs. Scale bars: 10 μm (a, d, f); 2 μm (e); 1 μm (g, h).

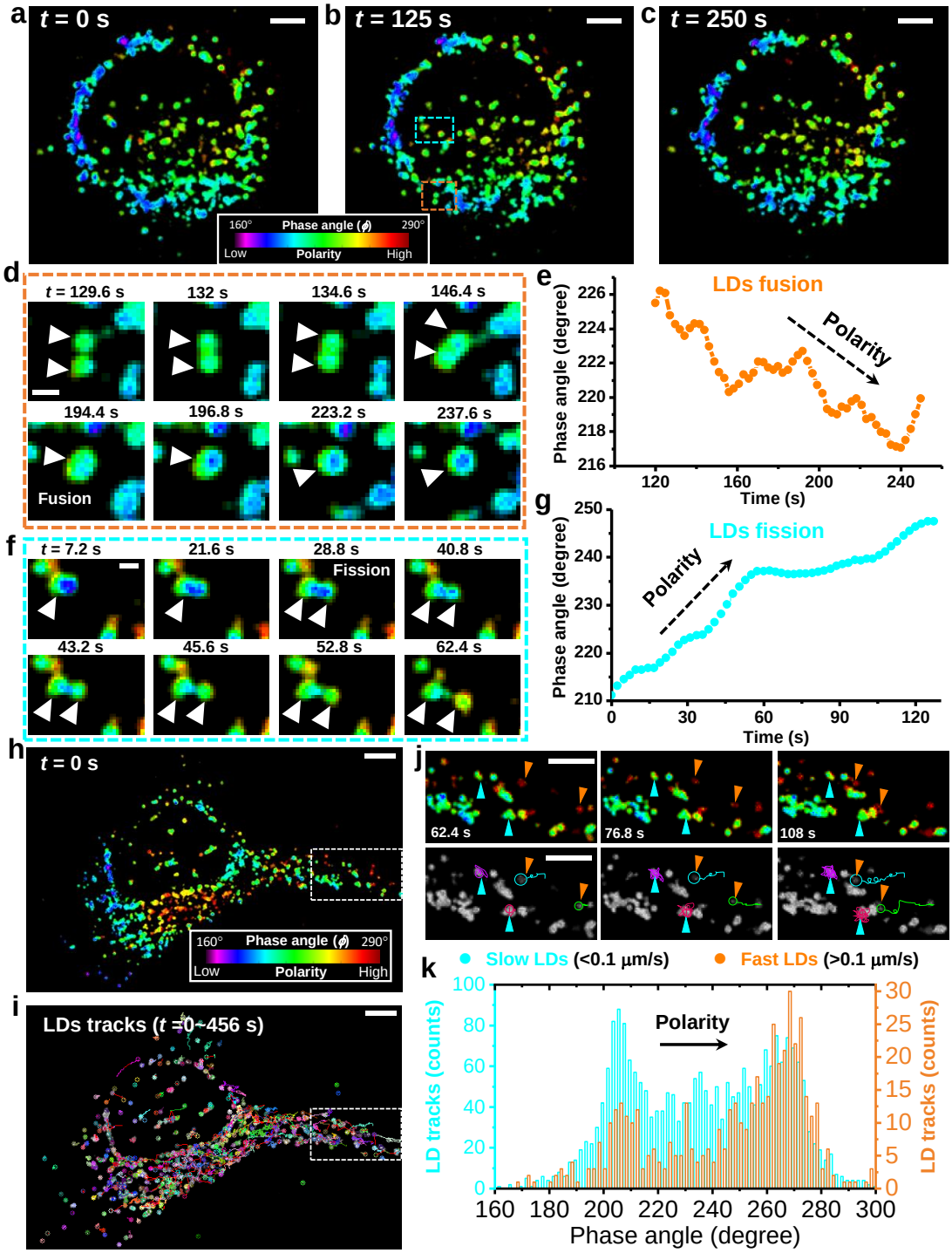

Figure 2. ExSPM unveils the spatiotemporal heterogeneities in polarity of LDs in live cells. a-c. ExSPM-derived LD polarity maps of a live COS-7 cell at different time points. **d**. Time sequences for the orange boxed region in b, showing LD fusion and associated polarity changes. **e.** Temporal variation in polarity for LDs indicated by arrowheads in d, highlighting a gradual polarity decrease during LD fusion. **f**. Time-lapse sequence of the cyan-boxed region in b, showing LD fission and associated polarity changes. **g.** Temporal variation in polarity for LDs indicated by arrowheads in f, highlighting a gradual polarity increase during LD fission. **h**. ExSPM-derived LD polarity map of another live COS-7 cell at *t* =0 s. **i**. Detected LDs and their local trajectories accumulated over 0–456 s, indicated by different colors. The movement of LDs were automatically tracked using a particle tracker model

(MosaicSuite, see Supplementary Video 5). **j**. Zoomed-in views of the boxed regions in h and i. Top: ExSPM-derived LD polarity map. Bottom: LDs tracks. Fast and high-polarity LDs are marked with orange arrowheads. Slow and low-polarity LDs are marked with cyan arrowheads. **k**. Distribution of measured phase angles (polarity) for fast (orange) and slow (cyan) LDs, classified based on a speed threshold of 0.1 μm/s. The experiments above were performed with 8-wavelength excitation cycles at 10fps. Each phasor image was generated by averaging three consecutive 8-frame sequences, resulting in an effective acquisition time of 2.4 s. Scale bar: 10 μm (a-c, h, i); 1 μm (d, f); 5 μm (j).

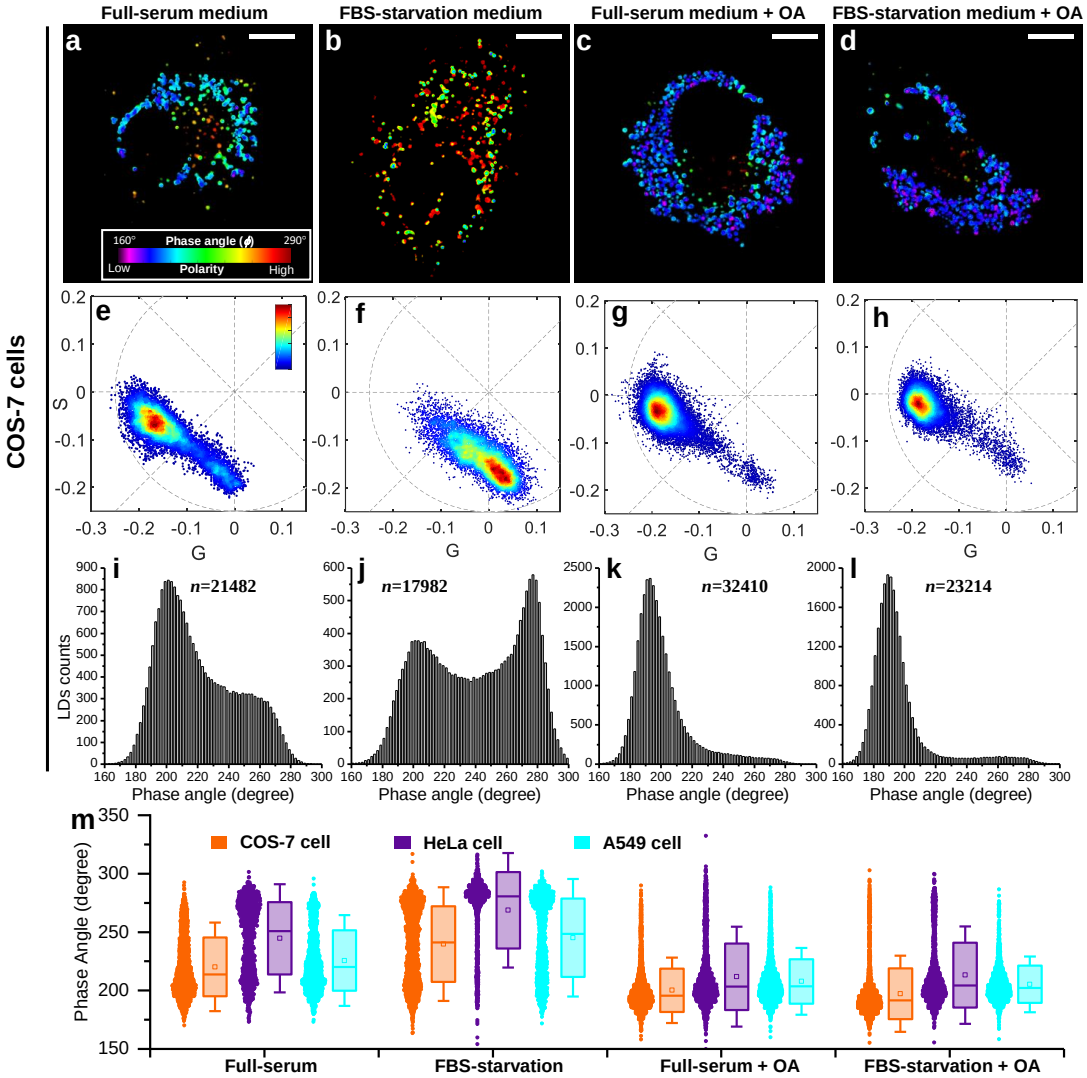

Figure 3. Assessment of LD polarity under different nutrient conditions using ExSPM. a-d. ExSPM-derived LD polarity maps of COS-7 cells cultured in full-serum medium (a), FBS-starvation medium (b), and 300 μM OA-supplemented media for 16h (c, d). **e-h.** Corresponding Phasor plot of the same excitation spectra data in a–d, providing a direct visualization of spectral shifts. **i-l.** Distributions of phase angles (polarity) for tens of thousands of LDs across 80-100 cells under the nutrient conditions in a–d. **m.** Statistical analysis of phase angles (polarity) across COS-7, HeLa, and A549 cells under different nutrient conditions. Scale bars:10 μm (a-d).

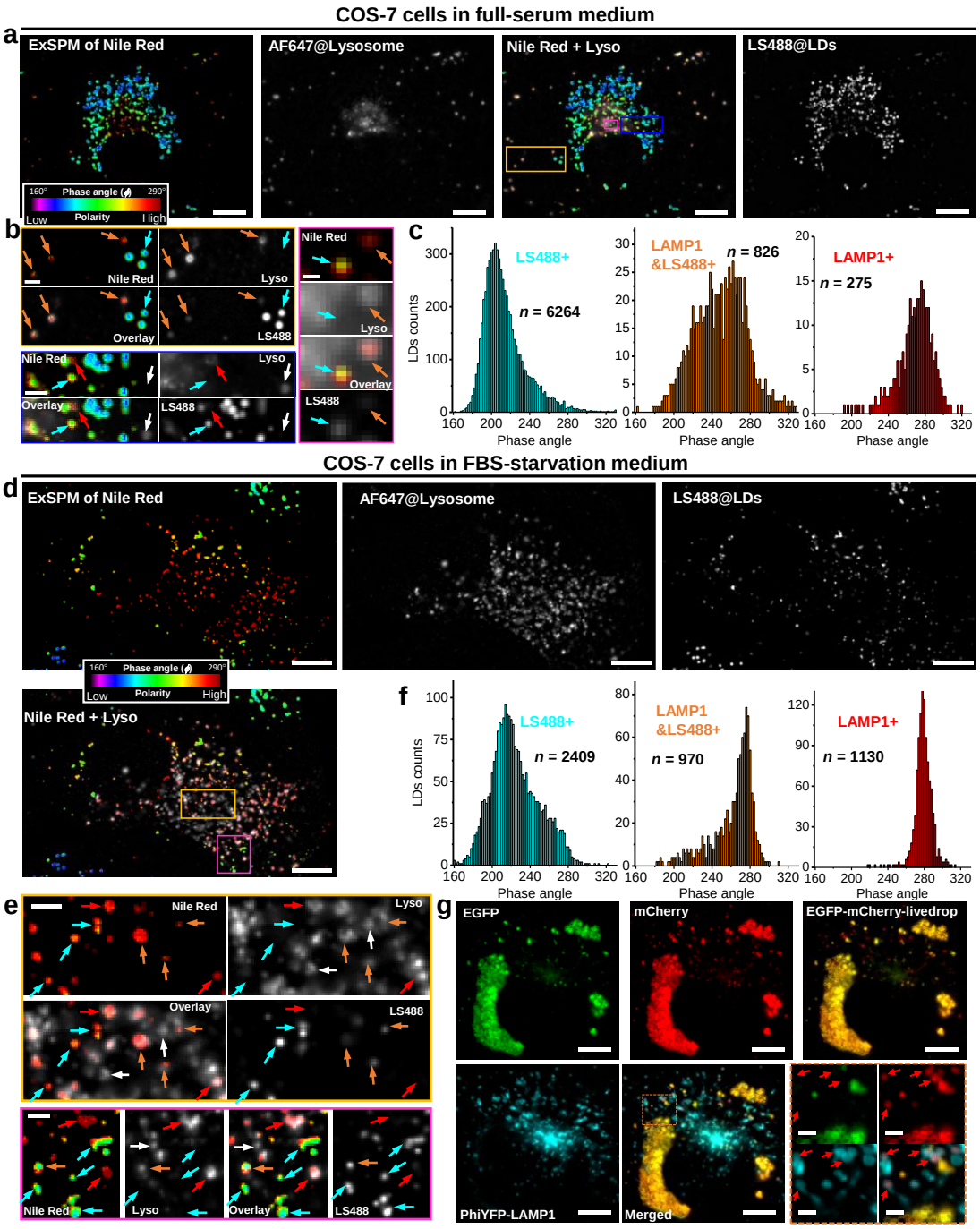

Figure 4. ExSPM unveils high-polarity LDs as a hallmark of lysosome-dependent acid lipolysis. a. Concurrent imaging of a COS-7 cell in full-serum medium, showing the ExSPM-derived LD polarity map (Nile Red staining), AF647-labeled lysosomes, and LipidSpot488 (LS488)-labeled LDs. **b.** Zoomed-in views of the boxed regions in a. Cyan arrows: LS488-only LDs; Orange arrows: LDs labeled by both LS488 and lysosomes; Red arrows: lysosome-only LDs; White arrows: free lysosomes not associated with LDs. **c.** Distribution of phase angles (polarity) for individual LDs across 30 cells, categorized by different markers (LS488, lysosomes, or both). **d.** Concurrent imaging of a COS-7 cell in FBS-starvation medium, showing the ExSPM-derived LD polarity map (Nile Red staining), AF647-labeled lysosomes, and LipidSpot488 (LS488)-labeled LDs. **e.** Zoomed-in views of the boxed regions in d. Cyan arrows: LS488-only LDs; Orange arrows: LDs labeled by both LS488 and lysosomes; Red arrows: lysosome-only LDs; White arrows: free lysosomes not associated with LDs. Both free lysosomes and lysosomes associated

with LDs significantly increased compared to these in a and b. **f.** Distribution of phase angles (polarity) for individual LDs across 20 cells, categorized by different markers (LS488, lysosomes, or both) as c. **g.** Concurrent ExSM imaging of mCherry-EGFP-livedrop and PhiYFP-LAMP1. Red arrows: Zoomed-in view of a region undergoing lipophagy, where only mCherry fluorescence was detected, while EGFP fluorescence was selectively quenched in acidic lysosomes. Scale bars: 10 μm (a, d, g); 2 μm (b, e, g); 0.5 μm for magnified view (magenta boxed region in b).

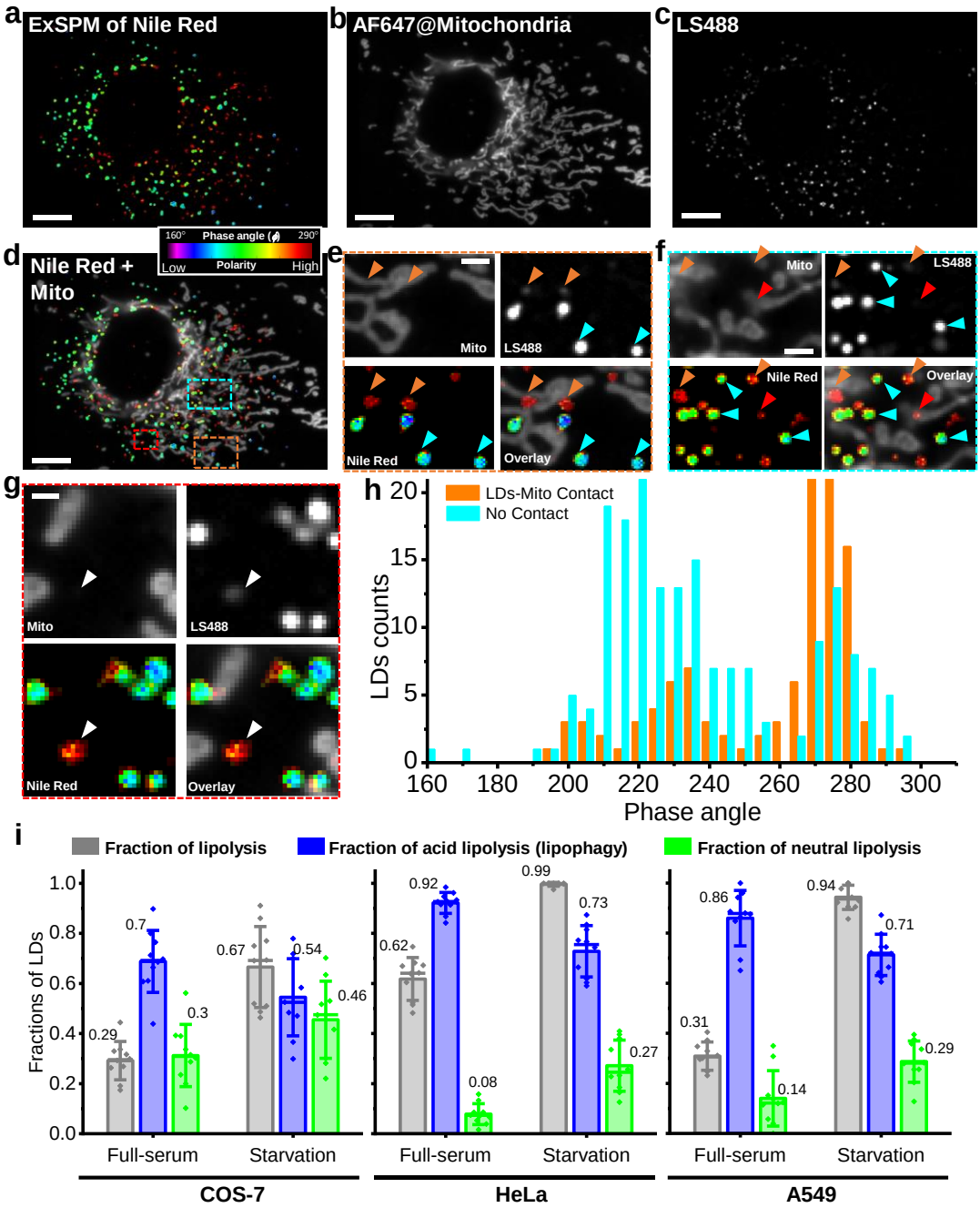

Figure 5. ExSPM unveils high-polarity LDs as a hallmark of neutral lipolysis through LD-mitochondria contacts. a-d. Concurrent imaging of a COS-7 cell in FBS-starvation medium, showing the ExSPM-derived LD polarity map (Nile Red staining) (a), AF647-labeled mitochondria (b), LipidSpot488 (LS488)-labeled LDs (c), and the overlay of polarity map and mitochondria (d). **e-f.** Zoomed-in views of the orange (e) and cyan (f) boxed regions in d. Cyan arrowheads: LS488-only LDs without mitochondria contacts. Orange arrowheads: LDs labeled by LS488 in contact with mitochondria. Red arrowheads: LDs in contact with mitochondria but without LS488 labeling. **g.** Zoomed-in views of the red boxed regions in d. White arrowheads: LS488-only LDs without mitochondria contacts but exhibiting high polarity. **h.** Distribution of phase angles (polarity) for individual LDs in the cell, categorized by the presence or absence of mitochondria contacts. **i.** Statistical analysis of fractions of LDs in COS-7 (left), HeLa (middle), and A549 (right) cells under nutrient-rich and deprivation conditions, each derived from analyses across 10 cells. Fraction of lipolysis refers to the proportion of lipolytic LDs relative to the total LDs in a cell. Fraction of

acid lipolysis represents the proportion of lipolytic LDs that co-localize with lysosomes relative to the total number of lipolytic LDs in a cell. Fraction of neutral lipolysis represents the proportion of lipolysis-active LDs that do not co-localize with lysosomes relative to the total number of lipolytic LDs in a cell. All the average fractions of each cell are indicated. Error bars, standard deviations between individual cells. Scale bars: 10 μm (a-d); 2 μm (e-f); 1 μm (g).